RSC Advances

PAPER

View Article Online
View Journal | View Issue



Cite this: *RSC Adv.*, 2026, **16**, 5179

# Biocompatible protein–nanomaterial scaffolds for controlled drug delivery

Bitopan Boro, [ac] Mridusmita Barman,[a] Rahul Sonkar, [ac] Punam Talukdar, [bc] Asis Bala [bc] and Devasish Chowdhury *[ac]

In this study, a series of collagen–hydroxyapatite (Col–HAp) composite scaffolds in the presence and absence of hexagonal boron nitride (h-BN) were fabricated using a controlled lyophilization technique to fabricate a functional biomaterial for drug delivery application. The lyophilization technique creates an interconnected porous network. The incorporation of h-BN in the Col–HAp/h-BN (1 : 2 : 1) scaffold prominently improved the mechanical strength of the scaffold, reaching 10.27 MPa as compared to the non-loaded h-BN scaffold, thereby enhancing its durability and structural stability. The loading of h-BN also displays a significant increase in surface area (47.27 $m^2$ $g^{-1}$), gaining abundant active sites for drug encapsulation. Circular dichroism (CD) spectroscopy confirmed the conformational behaviour of the collagen's secondary structure, indicating that in the presence of hydroxyapatite it preserved the native conformation and biological functionality. The Col–HAp/h-BN (1 : 2 : 1) scaffold revealed efficient ciprofloxacin (CIP) loading with a rate constant of 0.0719 $h^{-1}$ which follows the first order kinetics, while the release process followed a second order kinetic model with a rate constant of 3.24 $h^{-1}$, exhibiting a diffusion-based mechanism controlled by the scaffold's architecture. Enzymatic degradation assessment under a collagenase enzyme established that the Col–HAp/h-BN (1 : 2 : 1) scaffold underwent a gradual and sustained degradation pattern, as compared to other scaffolds, signifying that the incorporation of h-BN improved structural resistance and sustained biodegradability. In addition, biocompatibility studies revealed excellent cell viability, confirming the non-toxic and cytocompatibility nature of the scaffolds, validating the scaffold's safety for biological applications.

Received 25th November 2025
Accepted 16th January 2026

DOI: 10.1039/d5ra09090c

rsc.li/rsc-advances



## 1. Introduction

Scaffolds can be presented as implants or injections to deliver cells, drugs, and genes into the body. The scaffold provides a substrate for cell attachment, proliferation, differential function, and migration. Polymer scaffolds can take the form of a three-dimensional (3D) porous matrix, a nanofiber matrix, a thermosensitive sol–gel transition hydrogel, or a porous microsphere. Multifunctional scaffolds are prepared based on organic, inorganic, and mixed materials (organic–inorganic). The scaffolding materials must be biocompatible, tissue compatible, biodegradable, and capable of designing an appropriate scaffold with the required functionalities.[1] Natural materials, *e.g.*, alginate, proteins, collagens, gelatin, fibrins, and albumin, or synthetic polymers, *e.g.*, polyvinyl alcohol (PVA) and polyglycolide, can be used as scaffolds.[2,3]

Among all the polymers, collagen (Col) serves as a perfect basis for biomaterials considering their ready availability, nontoxicity, and native structure. The architecture and biochemical characteristics of collagens have been widely studied, and the latest literature reported that there were 28 collagen subtypes have been identified.[4,5] Nevertheless, the most remembered is type I collagen, the leading organic constituents of bone, tendon, and tooth. Consequently, collagen is regarded as one of the most beneficial natural biomaterials. In the biomedical field, collagen can be processed in scaffolding material, promoting cell migration, wound healing, and tissue regeneration.

Hydroxyapatite (HAp; $Ca_{10}(PO_4)_6OH_2$), the principal inorganic mineral component of bone and teeth, is extensively used in biomedical materials due to its excellent biocompatibility, bioactivity, osteoconductivity, and structural similarity to natural bone. The nanoscale architecture of HAp further enhances its biological relevance by promoting favourable interfacial interactions. However, the intrinsic brittleness and limited mechanical strength of HAp necessitate its integration with polymeric matrices to form composite scaffolds with improved mechanical stability and functional versatility.[6] Various advanced scaffolds, including chitin–HAp–collagen

[a]*Material Nanochemistry Laboratory, Physical Sciences Division, Institute of Advanced Study in Science and Technology, Paschim Boragaon, Garchuk, Guwahati, 781035, India. E-mail: devasish@iasst.gov.in; Fax: +91 361 2279909; Tel: +91 361 2912073*

[b]*Pharmacology and Drug Discovery Research Laboratory, Life Sciences Division, Institute of Advanced Study in Science and Technology, Paschim Boragaon, Garchuk, Guwahati, 781035, India*

[c]*Academy of Scientific and Innovative Research (AcSIR), Ghaziabad, 201002, India*

composites scaffolds,[7] Zn-doped mesoporous HAp microspheres,[8] magnetic HAp-based scaffolds,[9] PCL/HAp nanofiber matrices,[10] and multifunctional coatings like HAp-wollastonite-BN[11] have demonstrated enhanced structural integrity, mineralization potential, repairing bone defects, and bioactivity.

In recent years, nanofiller incorporation has emerged as an effective strategy to further enhance the performance of polymer–HAp composites. Nanofillers such as graphene oxide, silica nanoparticles, and carbon nanotubes have been explored extensively;[12] however, each presents limitations including oxidative instability, electrical conductivity, aggregation behaviour, or the need for extensive surface modification.[13] In contrast, hexagonal boron nitride (h-BN) offers a unique combination of high oxidation resistance, chemical inertness, thermal stability, and electrical insulation while maintaining stable interfacial interactions with polymeric and ceramic phases. These characteristics allow h-BN to act as an effective reinforcing agent without introducing electrical interference or chemical degradation. It is the lightest compound in group III–V, consisting of equal amounts of B and N atoms.[14] h-BN's ionic structure and high surface energy enable the binding of proteins that support cell adhesion (*e.g.*, fibronectin, vitronectin). This facilitates the imitation of biochemical indications that the ECM presents to the cell.[15] From a chemistry perspective, the performance of such composites is governed by interfacial interactions among the protein matrix, ceramic phase, and two-dimensional nanomaterial. Col protein functional groups can engage in hydrogen bonding, electrostatic interactions, and coordination with calcium ions in HAp, while the polar B–N bonds of h-BN facilitate stable non-covalent interactions at the interface. This synergistic interfacial chemistry plays a central role in determining the structural stability, molecular interactions, and functional performance of the resulting composite system.[16]

In the present work, we fabricated a series of three-dimensional (3D) composite scaffold by integrating collagen (Col), hydroxyapatite (HAp), and hexagonal boron nitride (h-BN) in varying ratios using the lyophilization process. As the h-BN is known for structural reinforcement characteristics and compatibility in composite biomaterials, the incorporation of h-BN was aimed to improve the bioactivity, mechanical performance and possible interfacial interactions. The resulting fabricated scaffolds were systematically characterized through different analytical techniques. Beyond their intrinsic bioactivity, the scaffolds signify excellent drug loading and release profile, demonstrating their potential in substantial therapeutic delivery applications. In addition, scaffold biodegradation behaviour was evaluated under collagenase enzymatic medium to mimic the physiological environment, providing insights into their resorption and stability. Biocompatibility is also initiated to further determine the suitability of the fabricated scaffold for biomedical applications.

# 2. Materials and methods

## 2.1. Materials

Collagen (bovine achilles tendon), hydroxyapatite, collagenase type I (clostridium histolyticum) and acetic acid (glacial) were obtained from Merck. Phosphate buffer saline (PBS, pH = 7.4) and hexagonal boron nitride (h-BN) nanopowder of average particle size 70 nm with a purity of 99.9% is procured from SRL Chemicals, India. Ciprofloxacin (CIP) was obtained from a local pharmacy store. Minimum Essential medium with non-essential amino acids (MEM-NAA) is purchased from Gibco. All chemicals were used without further purification. Distilled water was used throughout this study.

## 2.2. Methods

**2.2.1. Fabrication of Col–HAp/h-BN scaffold.** The fabrication of the scaffolds was carried out through a freeze-drying approach to achieve a highly porous architecture appropriate for biomedical applications.[17] In this study, four different types of scaffolds were fabricated to investigate the effect of composition and nanofiller incorporation. Initially, two Col–HAp scaffolds were prepared using different weight ratios of the components. For the first scaffold, 0.075 g of Col and 0.15 g of HAp were dispersed in 4 mL of 0.5 M acetic acid solution and stirred at 800 rpm with a magnetic stirrer at room temperature for 5 h, maintaining a Col–HAp weight ratio of 1 : 2. Similarly, a second scaffold was prepared in which the ratio was inverted to 2 : 1. These scaffolds were denoted as Col–HAp (1 : 2) and Col–HAp (2 : 1) respectively. Subsequently, two additional scaffolds were prepared by incorporating h-BN nanomaterials into the Col–HAp system. Specifically, 0.075 g of h-BN was added to the previously optimized Col–HAp (1 : 2) and Col–HAp (2 : 1) mixtures, yielding Col–HAp/h-BN (1 : 2 : 1) and Col–HAp/h-BN (2 : 1 : 1) scaffold, respectively. Following the preparation of the precursor dispersions, all the scaffold mixtures were subjected to deep freezing at −80 °C for 24 h in order to facilitate ice crystal formation within the network. After freezing, the samples were lyophilised under vacuum conditions, ensuring complete removal of ice crystal without structural collapse. The obtained dried scaffolds were stored at room temperature until further characterization and testing. The synthesis procedure of Col–HAp/h-BN scaffold was given in Scheme 1.

**2.2.2. Characterization of Col–HAp/h-BN scaffold.** The fabricated Col–HAp/h-BN nanocomposite scaffold were characterized by Fourier Transform Infrared (FTIR) spectroscopy (PerkinElmer Spectrum Two) in the range of 4000–400 $cm^{-1}$ for the analysis of the different functional groups using ATR mode with a spectral resolution of 0.5 $cm^{-1}$ and an average of 10 scans. The thermal stability of the scaffold was studied by a thermogravimetric analyser (TGA) PerkinElmer 4000 instrument. The scaffold sample was cut into small pieces and in each experiment, 5–10 mg of each scaffold was used for the TGA analysis with temperatures ranging from 35 to 800 °C under a nitrogen flow rate of 20 mL $min^{-1}$ with a pressure of 2 bar and at a heating rate of 10 °C $min^{-1}$. All the nitrogen adsorption–desorption isotherms of the fabricated scaffolds were obtained by using Brunauere– Emmett–Teller (BET) technique (Quantachrome iQ autosorb analyzer, USA). The average pore sizes of the samples were calculated as per the Barrett–Joyner–Halenda (BJH) approach. The morphological study of the fabricated Col–HAp/h-BN scaffold were performed using a Scanning Electron

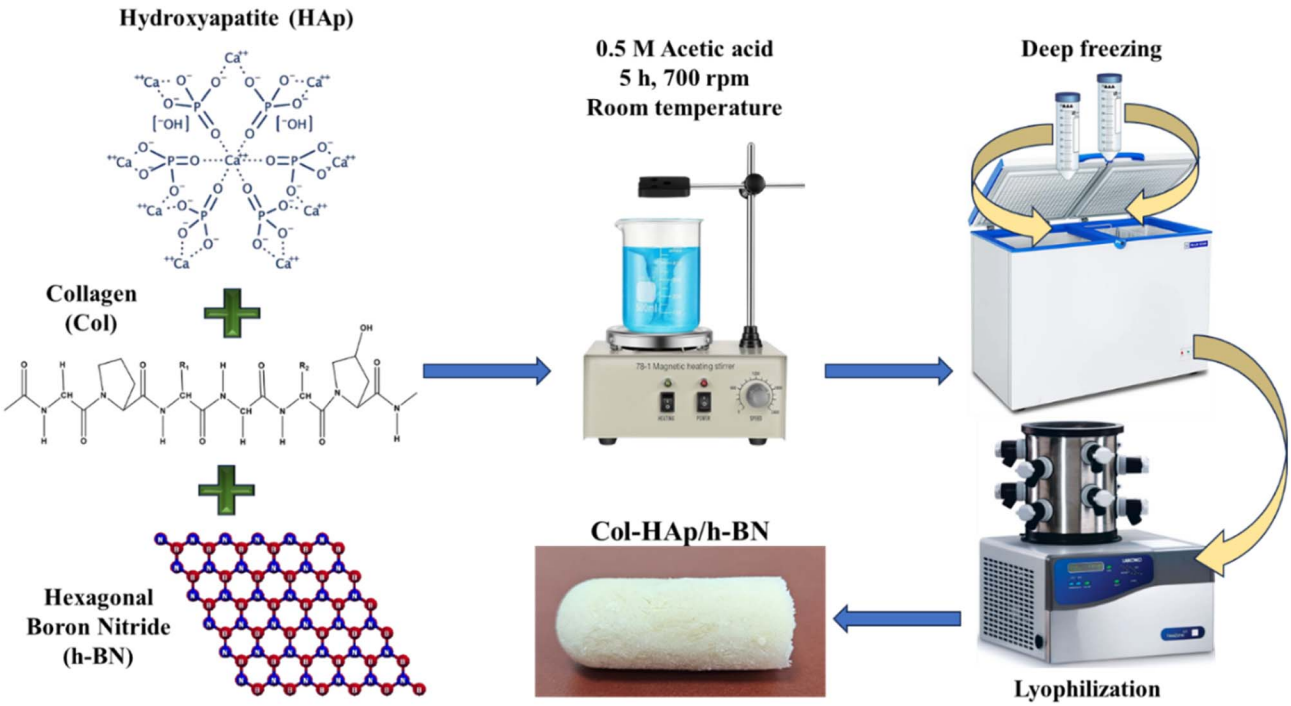


Scheme 1 Fabrication of the Col–HAp/h-BN scaffold.

Microscope (SEM) (make: Carl Zeiss ∑igma VP) and the existence of element within the scaffold was verified by the energy-dispersive X-ray spectroscopy (EDX).

**2.2.3. Mechanical property of the scaffold.** Unidirectional compression tests were conducted using a Tinius Olsen universal testing machine (model: H5KL) equipped with a 2.5 kN load cell, following the ASTM D695 standard.[18] Prior to testing, the lyophilised scaffolds were carefully trimmed using a sharp razor blade to level the top and bottom surfaces of all scaffolds ensuring uniform contact with the loading compression plates. The load cell was manually adjusted to a position roughly 11 cm above the test specimen using hydraulic controls. Cylindrical scaffold samples with diameter 12 mm, and thickness of 10 mm, were compressed between parallel plates at a constant strain rate of 5 mm $min^{-1}$. All samples were tested at room temperature in the dry state.

**2.2.4. Porosity measurement.** The porosity of the prepared Col–HAp (1 : 2, 2 : 1) and Col–HAp/h-BN (1 : 2 : 1, 2 : 1 : 1) scaffolds was measured by liquid displacement method.[5] Each of the scaffolds was immersed in ethanol for 5 min, and the porosity was calculated using the following eqn (1):

$$\text{Porosity} = (V_2 - V_1)/(V_2 - V_3) \times 100\% \quad (1)$$

where, $V_1$ = the initial volume of ethanol, $V_2$ = the total volume after adding scaffold into ethanol, $V_3$ = residual volume of ethanol after removing scaffold.

**2.2.5. Conformational study between Col and HAp through circular dichroism.** To quantify the conformational changes in the secondary structure of Col protein in the presence of HAp, circular dichroism (CD) spectra were studied. The CD values were acquired on a JASCO J-1100 spectrometer in the spectral range of 190–260 nm, using a quartz cuvette of 0.2 cm path length. The concentration of Col is 3 μM and HAp is 3 mg $mL^{-1}$ respectively. The experiment is done at 25 °C under a constant nitrogen flow of 5 standard litre per minute (slm). The secondary structure composition was assessed by analysing the raw spectral data using the online server BeStSel (beta structure selection, https://bestsel.elte.hu/index.php).[19]

**2.2.6. Degradation study of scaffold in collagenase enzymatic medium.** The enzymatic degradation of the fabricated Col–HAp/h-BN scaffolds was investigated by using a collagenase enzymatic solution prepared in phosphate buffer saline (PBS, pH 7.4) at a concentration of 0.2 mg $mL^{-1}$. Scaffolds of each composition were cut into uniform specimen with a diameter of 12 mm and a thickness of 2 mm, followed by immersion in the 5 mL of enzymatic solution. The scaffolds from each composition were removed after a regular interval of time and rinsed three times with deionized water to eliminate residual salts and enzyme traces and subsequently dried at room temperature. The percentage degradation of the scaffolds under enzymatic conditions was calculated according to eqn (2):[5,20]

$$\text{Degradation (\%)} = (W_0 - W_t)/W_0 \times 100\% \quad (2)$$

where $W_0$ is the initial and $W_t$ is the dry weight of scaffolds at different points in time.

**2.2.7. Drug load and release study of the scaffold.** The fabricated Col–HAp/h-BN (1 : 2 : 1) nanocomposite scaffolds were cut into cylindrical specimens with dimensions of 12 mm in diameter and 2 mm in thickness. Each specimen was immersed in a beaker containing 20 mL acetic acid solution (0.5

M) and incubated at room temperature for 1 h to activate the scaffold surface and improve its affinity toward drug molecules. After activation, the scaffolds were wisely dried in a hot air oven at 35 °C to remove excess solvent. The dried activated samples were subsequently immersed in a ciprofloxacin (CIP) drug solution of concentration 0.01 mg $mL^{-1}$ to facilitate drug loading experiment. The incorporation of the drug molecules into the scaffold was quantitatively monitored by UV-Vis spectrophotometer at a regular interval of time (30 min) in the wavelength range of 200 to 400 nm. The gradual decrease in the absorbance intensity of the CIP solution confirms the encapsulation of drug molecules into the scaffold matrix, thereby suggesting their potential as an efficient drug delivery platform.

The CIP loaded Col–HAp/h-BN (1 : 2 : 1) scaffolds were subsequently used for the evaluation of their drug release behaviour. For this study, the drug loaded scaffolds were immersed in the distilled water (pH = 7), which serve as the release medium under physiological conditions. The concentration of CIP release into the medium was quantitatively monitored at an interval of 30 min using a UV-Vis spectrophotometer in the wavelength range of 200–400 nm. The gradual increase in the absorbance intensity of the release medium confirmed the diffusion of CIP drug molecules from the scaffold matrix in the surrounding solution, thereby reflecting as drug the delivery platform.

#### 2.2.8. Biocompatibility study of the scaffolds

*2.2.8.1. Maintenance of cell line.* The McCoy (mouse fibroblast) cell line was procured from the National Centre for Cell Science (NCCS), Pune, India. Upon arrival, the cells were maintained under aseptic conditions in the institute's cell culture laboratory. They were cultured at 37 °C in MEM NAA medium supplemented with 10% fetal bovine serum (FBS) and 1% antibiotic–antimycotic solution. The cultures were incubated in a regulated environment comprising 95% air and 5% (v/v) $CO_2$.

*2.2.8.2. Sterilisation of scaffolds.* The scaffolds studied for the cell viability assay was initially cut into small pieces with a diameter of 2 mm and a thickness ranging from 0.6 to 0.8 mm. These samples were then sterilized by immersion in 70% ethanol for 2 h, followed by exposure to UV radiation for 1 h inside an Eppendorf biosafety cabinet. Post-sterilization, the samples were incubated overnight in MEM-NAA complete medium to facilitate equilibration.

*2.2.8.3. MTT assay.* When the cultured cells reached approximately 80% confluency in the culture flask, cells at passage number 20 were transferred into a 96 well polystyrene plate (Tarson, India) at a seeding density of $5 \times 10^4$ cells per mL and incubated for 24 h. Following this incubation period, the sterilized test samples were carefully introduced into the wells containing the adherent cell monolayer and further incubated for another 24 h under identical conditions. After the treatment period, the culture medium was gently aspirated, and each well received 90 μL of fresh medium along with 10 μL of MTT solution (12 mM, prepared at 5 mg $mL^{-1}$ in PBS and filter sterilized).[21] The plates were then incubated at 37 °C for 4 h to allow viable cells to enzymatically reduce the MTT reagent into insoluble formazan crystals.[22] Subsequently, 50 μL of dimethyl sulfoxide (DMSO) was added to each well to dissolve the formazan, followed by a 10 min incubation at 37 °C to ensure complete solubilization. The cell viability was quantified by measuring the absorbance at 540 nm using a microplate reader, with the values normalized against the untreated control group.

## 3. Results and discussion

### 3.1. Characterization of the Col–HAp/h-BN scaffold

The Col–HAp scaffold with h-BN, with varying concentrations of Col and HAp, namely Col–HAp (1 : 2), Col–HAp/h-BN (1 : 2 : 1), Col–HAp (2 : 1), and Col–HAp/h-BN (2 : 1 : 1) displayed a uniform cylindrical shape measuring approximately 3.0–4.5 cm in length and approximately 1.2–1.3 cm in diameter. The scaffolds appeared spongy in nature, revealing an interconnected porous structure, yet maintain a compact and tight form, demonstrating an adequate structural stability. The morphological balance between porosity and mechanical integrity of the scaffold is advantageous for therapeutic delivery applications, as it enables efficient drug uptake and controlled release profile while preserving sufficient stability for administration and sustained therapeutic action. The digital photographs of the fabricated scaffold are shown in Fig. 1(A) which appears to be white in colour.

**3.1.1 FTIR analysis.** The FTIR spectra of the fabricated scaffolds Col–HAp (2 : 1), Col–HAp/h-BN (2 : 1 : 1), Col–HAp (1 : 2), and Col–HAp/h-BN (1 : 2 : 1) are shown in Fig. 1(B), which is recorded in the range of 4000–400 $cm^{-1}$. The functional groups present in Col, HAP and h-BN exhibit various characteristic peaks. All the spectra exhibit stretching vibrations for hydroxyl (–OH) group at 3303 $cm^{-1}$ and amine (–NH) groups, both overlapping with each other. This peak is more intense in Col–HAp (2 : 1), denoting strong H-bonding interactions between Col and HAp. The C–H stretching vibration was observed at peak 2930 $cm^{-1}$, originating from the aliphatic side chains of the Col protein backbone.[23] This peak is more distinct in h-BN containing samples, particularly Col–HAp/h-BN (2 : 1 : 1) and Col–HAp/h-BN (1 : 2 : 1), indicating a reduced exposure to surface functional groups or a more compact structure. Characteristic amide I (C=O stretching) and amide II (N–H bending) bands of Col protein are shown by peaks 1652 $cm^{-1}$ and 1552 $cm^{-1}$, respectively.[24,25] In Col–HAp (1 : 2), a strong protein–BN interaction is not present, as no h-BN is added, and the β-sheet arrangement of Col protein is retained. When h-BN is incorporated in Col–HAp/h-BN (1 : 2 : 1), the peak at 1639 $cm^{-1}$ becomes more prominent, suggesting h-BN and polymer matrix interactions.[26] The amide I peak at 1645 $cm^{-1}$ for Col–HAp (1 : 2) shifts slightly to 1652 $cm^{-1}$ in Col–HAp/h-BN (2 : 1 : 1), indicating potential structural rearrangements within the polymer matrix. The increase in intensity of B–N characteristic peaks denote the effective amalgamation and interaction of h-BN with the scaffold. The peaks related to phosphate ($PO_4^{3-}$) stretching vibrations from HAp appeared in the spectra of all scaffolds around 1240, 544, and 659 $cm^{-1}$. These peaks are sharp and distinct in all the samples, suggesting that the crystallinity of the HAp is maintained when h-BN is incorporated.[27,28] The peak at 872 $cm^{-1}$ corresponds to B–N stretching vibration, and

 

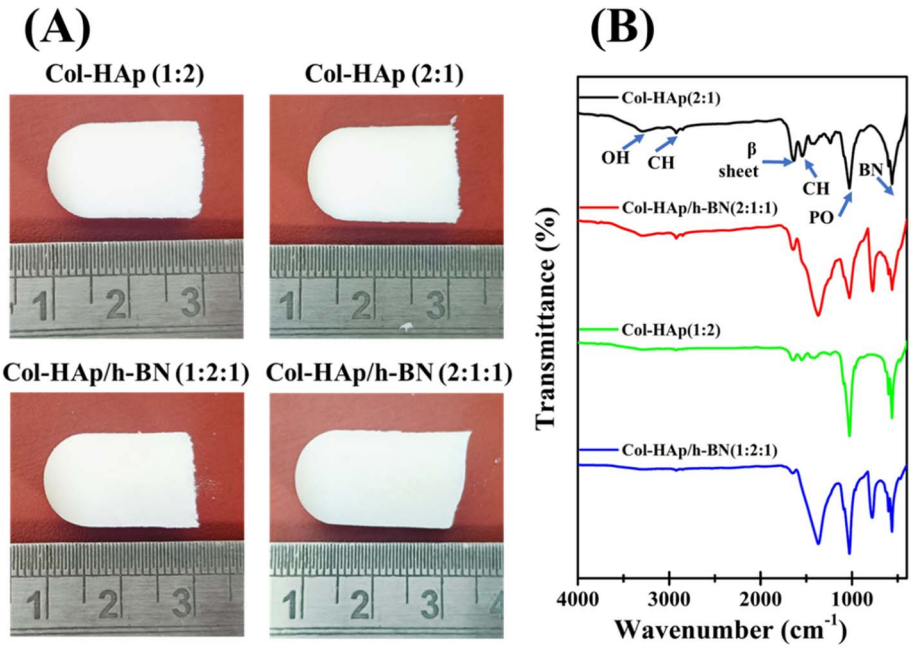


Fig. 1 (A) Digital images of the scaffold and (B) FTIR spectra of different scaffold.

1330 $cm^{-1}$ is attributed to bending modes of B–N–B. Such peaks are more pronounced in Col–HAp/h-BN (1 : 2 : 1) and Col–HAp/h-BN (2 : 1 : 1) with higher h-BN content. Altogether, these peaks confirm the successful interaction of h-BN within the biopolymer matrix, as well as cross-linking between the constituents of the scaffolds. The formation of intermolecular interactions between the Col–HAp and h-BN, plays a key role in improving interfacial adhesion, which directly translates into improved load-bearing capability and structural integrity of the scaffolds. The FTIR analysis confirms the presence of functional groups capable of interacting with drug molecules, which is critical for governing drug loading efficiency and release behaviour in drug delivery applications.

**3.1.2. TGA analysis.** The thermal degradation behaviour, demonstrating the weight loss (%) as a function of temperature up to 800 °C shown by the scaffolds consisting of varying concentrations of Col, HAp and h-BN was evaluated by thermogravimetric analysis (TGA). The TGA graphs of the samples with scaffolds Col–HAp (2 : 1), Col–HAp/h-BN (2 : 1 : 1), Col–HAp (1 : 2), and Col–HAp/h-BN (1 : 2 : 1); are shown in Fig. 2(A). The TGA profiles for all the scaffolds follow a multi-step degradation process, observing a typical thermal decomposition stage associated with biopolymer-based materials. The initial weight loss is below 150 °C where the percentage of weight loss of samples of Col–HAp (1 : 2), and Col–HAp/h-BN (1 : 2 : 1) is almost the same, around 8% and both follows the same TGA pattern, while that of Col–HAp (2 : 1) is 10% and Col–HAp/h-BN (2 : 1 : 1) is 4%. Such weight loss is due to the evaporation of the absorbed moisture and loosely bound water molecules. This weight loss is more evident in the Col–HAp (2 : 1) sample, may be due to relatively loose matrix or less cross-linking due to the higher amount of Col protein concentration in the scaffold.[29] The second notable degradation phase where most prominent weight loss is observed, occurs between the temperatures 200 °C and 400 °C. In this phase, decomposition of Col protein occurs, which includes the breakdown of the peptides and release of small organic compounds. Among these scaffolds, Col–HAp/h-BN (1 : 2 : 1) sample with less Col protein concentration demonstrates the least pronounced weight loss (22%) as compared to the other samples Col–HAp (1 : 2) (23%), Col–HAp (2 : 1) (35%), and Col–HAp/h-BN (2 : 1 : 1) (35%). Thus, Col–HAp/h-BN (1 : 2 : 1) shows higher thermal resistance, highlighting higher structural stability than Col–HAp (2 : 1), Col–HAp/h-BN (2 : 1 : 1), and Col–HAp (1 : 2).[30,31] The last stage, stretching from 400 to 700 °C, involves the degradation of more stable residues like cross-linked networks, and other remaining inorganic content. The percentage of weight loss is around 8% for Col–HAp (2 : 1), followed by 4% and 1% for Col–HAp (1 : 2) and Col–HAp/h-BN (2 : 1 : 1) scaffold respectively. Col–HAp/h-BN (1 : 2 : 1) shows no weight loss, suggesting that the scaffold's organic part has decomposed before 400 °C, and the remaining materials are thermally very stable.[32] The thermogravimetric analysis of the Col–HAp/h-BN scaffolds reveal that the inclusion of lower amount of Col protein and higher HAp with the inclusion of h-BN in the ratio 1 : 2 : 1 improves the thermal stability of the materials. The residual weight of Col–HAp/h-BN (1 : 2 : 1) is 71.4%, Col–HAp (1 : 2) is 60%, Col–HAp/h-BN (2 : 1 : 1) is 53.8%, and Col–HAp (2 : 1) is around 42.9%. Hence, while the samples exhibit a typical multi-step degradation observed in polymeric systems, the highest residual mass is observed in Col–HAp/h-BN (1 : 2 : 1) sample. This result supports the potential application of h-BN-reinforced Col–HAp scaffolds in drug delivery.

**3.1.3. BET analysis.** To examine the specific surface area, pore dimensions, and the relationship between surface and pore characteristics of a scaffold used for drug delivery,

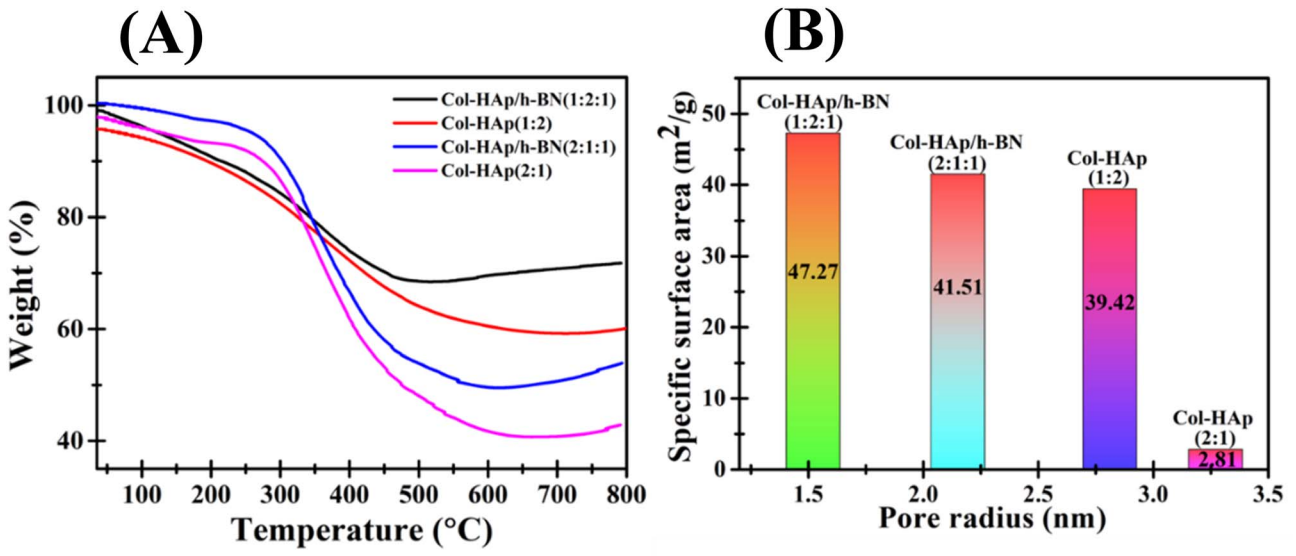


Fig. 2 (A) TGA and (B) pore radius *vs.* Surface area graph of different scaffold.

catalysis, and energy storage applications, the Brunauer–Emmett–Teller (BET) analysis using a gas adsorption–desorption isotherm is critical. We measured the $N_2$ adsorption–desorption isotherms of all four fabricated scaffold samples at 60 °C while maintaining a continuous flow of nitrogen for 10 h. The Fig. S1 depicts the obtained $N_2$ adsorption/desorption isotherms for each sample. The BET surface analyser was used to assess the specific surface area and pore radius of the as-fabricated samples. It was found that the adsorption of nitrogen gas grew slowly until the relative pressure reached around a value of 0.80 for each sample, and then a sudden increase was detected when the relative pressure crossed the value of 0.80. All three recorded isotherms were found to match a typical type IV isotherm, confirming the presence of a mesoporous structure within the scaffold matrix. The introduction of h-BN nanomaterial within the scaffold resulted in a considerable improvement in surface area, while the pore diameters gradually decreased. The resultant enhancement in specific surface area of the Col–HAp/h-BN (1 : 2 : 1) scaffold significantly promotes their dispersion in a solution and boosted their potential for targeted drug delivery applications. We have evaluated the specific surface area of 47.27 $m^2 g^{-1}$, 39.42 $m^2 g^{-1}$, 41.51 $m^2 g^{-1}$, and 2.82 $m^2 g^{-1}$ together with pore radius of 1.5 nm, 2.8 nm, 2.15 nm, and 3.2 nm, respectively, for Col–HAp/h-BN (1 : 2 : 1), Col–HAp (1 : 2), Col–HAp/h-BN (2 : 1 : 1), and Col–HAp (2 : 1) scaffold sample. The obtained specific surface area *vs.* pore radius was expressed in a histogram for each sample, as shown in the Fig. 2(B). The reduced pore size in scaffold is beneficial for promoting specific cellular uptake and tissue regeneration processes. Nanoscale level pores enhance the adsorption of bioactive molecules, which are essential for the initial proliferation and adhesion of osteoblasts and fibroblasts on the scaffold surface. The increased surface area related with these fine pores enable extracellular matrix (ECM) formation, ion exchange, and biomineralization, creating a bioactive interface that supports early osteogenic activity. Mukasheva *et al.* (2024) reported that,[33] pore sizes in the range of 50–100 μm are most suitable for osteoblast attachment and bone matrix formation, while larger pores between 200–400 μm favour vascularization and deep bone ingrowth. Smaller pores (<10 μm) assist in fibroblast growth and ECM deposition, whereas intermediate pores (20–80 μm) are helpful for epithelial and endothelial cell proliferation. Therefore, the integration of nanoporous surfaces enhances the biochemical interactions and macroporous structures that facilitates cell migration and nutrient flow providing a synergistic environment suitable for bone tissue regeneration and localized drug delivery applications. The Col–HAp/h-BN (1 : 2 : 1) scaffold, possessing the smallest pore size, offers a higher surface area that facilitates controlled and sustained drug release, making it a promising candidate for targeted drug delivery applications.

**3.1.4. SEM and EDX analysis.** The microstructural and compositional analysis of the fabricated different scaffolds at varying ratios demonstrates the direct influence of composition on scaffold morphology, porosity, and surface chemistry, as revealed by SEM and EDX results shown in Fig. 3. In the Col–HAp (1 : 2) scaffold represented in Fig. 3(A) and (A′), a greater proportion of HAp shifts the morphology towards a mineral-dominated character. SEM images display rougher surfaces and irregular elongated pore channels. EDX spectra displays in Fig. 3(C) supports the presence of O (39.32%, 39.26%), P (5.43%, 2.80%), and Ca (13.58%, 5.41%). The absence of boron and nitrogen peaks validates this as a control sample without h-BN incorporation. The introduction of h-BN in the Col–HAp/h-BN (1 : 2 : 1) scaffold depicted in Fig. 3(B) and (B′) noticeably alters the morphology. SEM reveals broader and less spherical pores with rougher and thicker pore walls, arising from the integration of layered h-BN nanosheets into the Col–HAp matrix. The nanosheets displays increased surface roughness and structural complexity, which would provide more binding

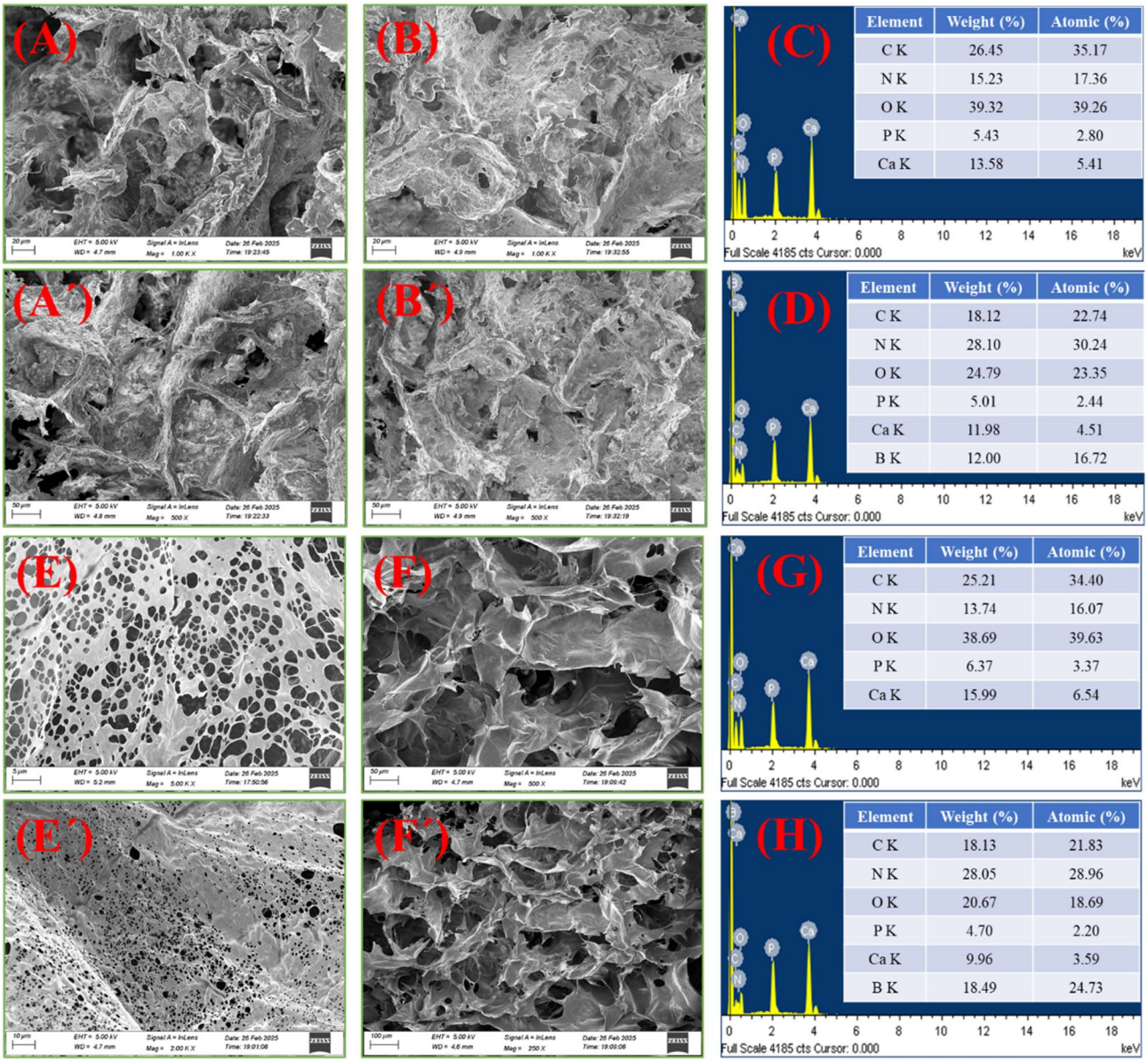


Fig. 3 SEM images of scaffold of Col–HAp (1 : 2) at (A) high and (A′) low magnification, Col–HAp/h-BN (1 : 2 : 1) at (B) high and (B) low magnification, Col–HAp (2 : 1) at (E) high and low magnification, Col–HAp/h-BN (2 : 1 : 1) at high and low magnification. The corresponding EDX spectra of Col–HAp (1 : 2), Col–HAp/h-BN (1 : 2 : 1), Col–HAp (2 : 1), and Col–HAp/h-BN (2 : 1 : 1) are presented in (C), (D), (G), and (H), respectively (the inset table in each spectrum shows the percentage of elemental composition of each scaffold).

sites for drug encapsulation. EDX spectra shown in Fig. 3(D) further reinforce this with N (28.10%, 30.24%) and B (12.00%, 16.72%) peaks from h-BN, accompanied by reduced C (18.12%, 22.74%), and significant O (24.79%, 23.35%), P (5.01%, 2.44%), and Ca (11.98%, 4.51%). These values confirm h-BN incorporation and the dominance of HAp in the scaffold matrix.

For Col–HAp (2 : 1), the SEM micrographs show in Fig. 3(E) and (E′) illustrate a highly porous, interconnected structure characterized by uniformly distributed rounded and oval pores. The dense Col protein framework interspersed with HAp particles produces a balanced fibrous-mineral network. EDX spectra shown in Fig. 3(G) confirm the dual-phase composition with predominant C (25.21%, 34.40%) and O (38.69%, 39.63%) reflecting the Col protein matrix, along with P (6.37%, 3.37%) and Ca (15.99%, 6.54%) corresponding to HAp.[5,34] On the other hand, the Col–HAp/h-BN (2 : 1 : 1) shown in Fig. 3(F) and (F′) scaffold reveals the most heterogeneous and rugged microstructure of all formulations. SEM demonstrates large, irregular pores with clear evidence of h-BN nanosheet agglomerations. EDX spectra depicted in Fig. 3(H) supports these changes, with N (28.05%, 28.96%) and B (18.49%, 24.73%) peaks confirming h-BN incorporation. The relative decrease in C (18.13%, 21.83%) and Ca (9.96%, 3.59%) highlights the displacement of Col protein and HAp by h-BN. O (20.67%, 18.69%) and P (4.70%, 2.20%) however, remain significant, indicating retention of the mineral phase alongside h-BN. Thus, pure Col–HAp scaffolds provide balanced fibrous-mineral matrices with uniform porosity, while the inclusion of h-BN transforms the

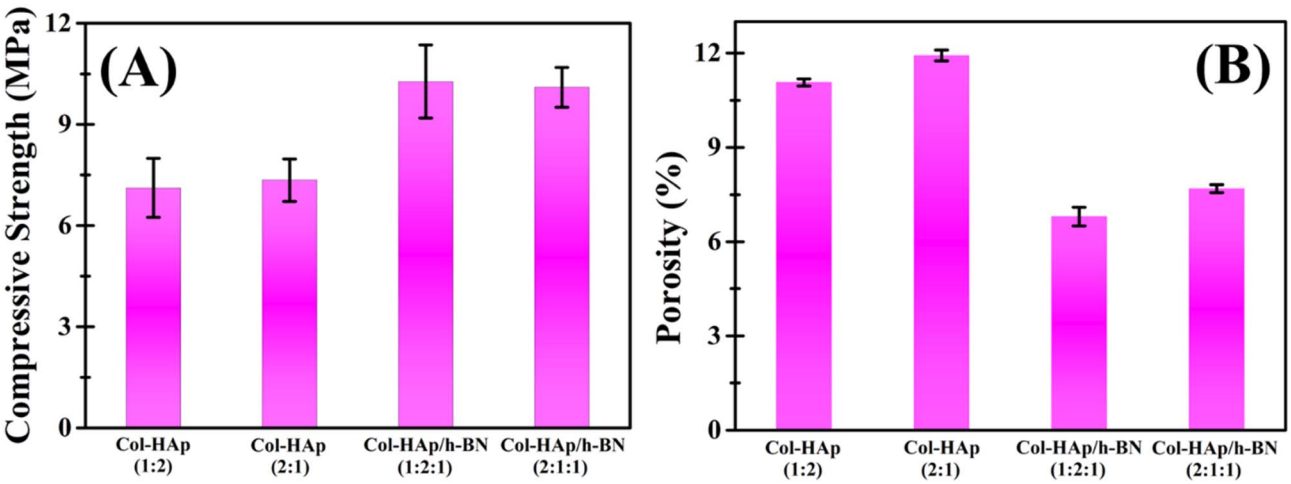


Fig. 4 (A) Compressive strength and (B) porosity percentage of different scaffold.

morphology, creating rougher, more heterogeneous pore structures. Overall, the SEM and EDX results suggest that h-BN reinforced Col–HAp scaffolds offer enhanced porosity and greater potential for drug delivery. Furthermore, the interconnected porous architecture and uniform pore distribution observed in the h-BN reinforced scaffolds are expected to facilitate effective stress transfer within the matrix, thereby contributing to the enhanced mechanical stability observed at the macroscopic scale.

### 3.2. Mechanical property of the scaffold

Fig. 4(A) illustrates the compressive strength of all the fabricated scaffolds, reflecting the effect of the compositional variation and incorporation of h-BN nanomaterial on the performance of mechanical stability. The as fabricated Col–HAp (1 : 2) and Col–HAp (2 : 1) scaffolds exhibited compressive stress values of 7.12 ± 0.872 and 7.34 ± 0.625 MPa respectively, signifying the Col–HAp ratio plays an important key role in determining the load bearing capacity of the scaffold. Upon incorporation of h-BN as nanofiller the compressive strength of the scaffolds improved significantly, with a value of 10.27 ± 1.081 MPa for Col–HAp/h-BN (1 : 2 : 1) and 10.10 ± 0.592 MPa for Col–HAp/h-BN (2 : 1 : 1) scaffolds. This improvement can be attributed to the effective stress distribution and interfacial reinforcement convey by h-BN nanomaterial, which acts as a mechanical support system for the scaffold. The presence of h-BN nanomaterial contributes to the defect healing mechanism by reducing the overall porosity of the scaffold which is confirm by the BET analysis that displays a smaller pore radius for the h-BN incorporation scaffold compared to Col–HAp, indicating a denser and more compact microstructure that contribute to enhanced mechanical performance. The Table 1 represents the values of compressive stress of different scaffolds. The observed enhancement in compressive strength upon incorporation of h-BN nanomaterial aligns with the previous reports on polymer-ceramic and Col–HAp based scaffolds, where the inclusion of nanofillers significantly improves mechanical performance by enhancing the interfacial bonding within the matrix. Similar type of effects have been reported in Col/HAp nanocomposites reinforced with silica nanoparticles and graphene oxide, where the nanofillers effectively occupy the microvoids architecture and refine the pore network, resulting in increased load distribution and higher mechanical performance.[35,36] The reduction in pore size and the compact structure observed in the present study are consistent with the BET analysis, which confirmed the densification effect caused by the h-BN incorporation. This densification reduces the overall stress and enables the uniform stress transmission throughout the scaffold matrix, leading to a significant enhancement in compressive strength. The all-fabricated scaffolds demonstrated compressive strength values within the optimal range of 7 to 10 MPa, which corresponds to the mechanical strength of natural trabecular bone. The improved compressive performance of the h-BN reinforced scaffolds can be directly correlated with the refined pore morphology and strengthened interfacial interactions at the microscale, highlighting the strong structure property relationship within the developed system. Therefore, the integration of Col, HAp and h-BN effectively enhances the mechanical performance without compromising biocompatibility, underscoring their potential application in bone tissue engineering as well as in drug delivery application.

### 3.3. Porosity measurement

Porosity act as an important role in finding the biological and mechanical performance of scaffolds. It can regulate the nutrient diffusion, cell infiltration, and tissue regeneration, as

Table 1 Compressive stress values of different scaffold (mean ± standard deviation (SD))

| Scaffolds | Col–HAp (1 : 2) | Col–HAp (2 : 1) | Col–HAp/h-BN (1 : 2 : 1) | Col–HAp/h-BN (2 : 1 : 1) |
|---|---|---|---|---|
| Compressive stress (MPa) | 7.12 ± 0.872 | 7.34 ± 0.625 | 10.27 ± 1.081 | 10.10 ± 0.592 |

well as influencing drug loading/release and degradation pattern. The biological activity enhances depending on the high porosity of the scaffold by providing interconnected pathways for cell migration and vascularization while it may reduce the overall mechanical strength. Conversely, lower porosity improves the structural integrity and stability but it can limit the permeability of therapeutic agents. Therefore, achieving an optimal porosity is essential to balance biological functionality and mechanical stability, which make them a key parameter for designing smart scaffold for bone tissue engineering and drug delivery applications.[33] Fig. 4(B) reflects the porosity percentage of the fabricated scaffolds with different compositions of Col protein, HAp and h-BN nanomaterial. The porosity results clearly reveal a compositional dependence of the scaffold microstructure. The Col–HAp (2 : 1) scaffold exhibited the highest porosity of 11.92%, followed by Col–HAp (1 : 2) (11.07%), whereas the incorporation of h-BN led to a significant decrease in porosity for both hybrid formulations. The Col–HAp/h-BN (1 : 2 : 1) scaffold showed the lowest porosity of 6.8%, while Col–HAp/h-BN (2 : 1 : 1) displayed a moderate value of 7.69%. The higher porosity observed in the pure Col–HAp scaffolds can be attributed to the existence of an open and loosely packed polymer–ceramic network. The interaction between Col protein and HAp produces a porous framework with interconnected voids, which is advantageous for nutrient diffusion, cell attachment, and tissue formation. However, the inclusion of h-BN nanosheets led to a denser and more compact structure, reducing the total pore volume. This decrease in porosity is primarily due to the filling of interstitial spaces between Col protein and HAp particles by the 2D h-BN nanofillers, which promotes the matrix packing and minimize void formation. The h-BN nanosheets act as reinforcing bridges at the Col–HAp interface, improving the structural compactness and decreasing pore interconnectivity. The resultant porosity range (6–12%) indicates that all scaffolds retain a suitably porous structure that can support biological activity while maintaining sufficient mechanical stability. The tunable porosity achieved through h-BN addition demonstrates that the internal architecture of the Col–HAp scaffold can be effectively tailored to balance biological performance and structural strength, making these composites promising candidates for bone tissue engineering and controlled drug delivery applications.

### 3.4. Conformational study between Col and HAp

The folding and unfolding nature of Col protein in the presence of HAp was thoroughly investigated using circular dichroism (CD) spectroscopy and is shown in Fig. 5(A). This spectral shift is further substantiated by secondary structure content analysis using the BeStSel deconvolution method.[19] Native Col protein exhibited a distinct negative peak near 199 nm and a weak positive band around 225 nm, characteristic of the triple-helical conformation that maintains the protein's folded state. From Table 2, the corresponding secondary structure study revealed a dominant β-sheet content (76.5%), moderate α-helical content (13.5%), and minimal disordered or turn regions, confirming a highly folded and structurally stable protein conformation in its native state. This spectral pattern is typical for Col protein's triple-helical structure and arises predominantly from poly-proline II (PPII) helical arrangements and β-sheet-like extended conformations stabilized by interchain hydrogen bonding. The negative band corresponds to π–π* transitions of peptide bonds in an ordered, chiral helical structure, while the positive region is attributed to n–π* transitions related to non-random coil conformations.[37] Upon the incorporation of HAp,

Table 2 Percentage of secondary structural content of Col protein in the presence and absence of HAp

| Sample | α-Helix (%) | β-Sheet (%) | Turn (%) | Others (%) |
|---|---|---|---|---|
| Collagen (Col) | 13.5 | 76.5 | 4.3 | 5.7 |
| Col–HAp | 1.0 | 45.6 | 14.0 | 39.4 |

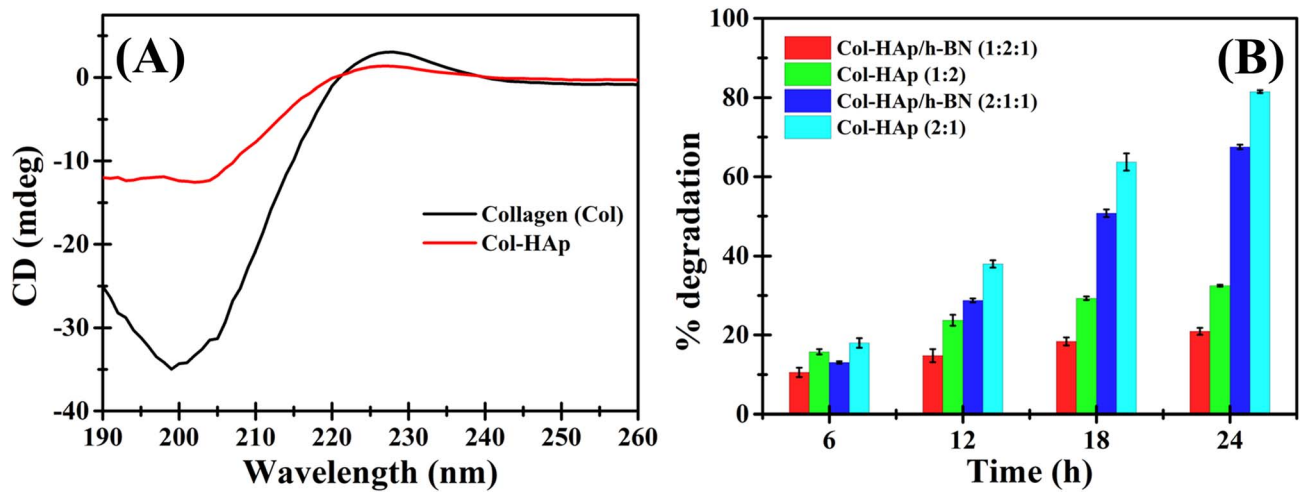


Fig. 5 (A) CD spectra of Col protein and in presence of HAp, (B) scaffold degradation under collagenase enzymatic medium.

a significant reduction in ellipticity and band intensity was observed, suggesting partial unfolding of the triple-helical structure and disruption of the protein's native conformation.

The quantitative percentage analysis of secondary structure composition further supports this observation. As shown in Table 2, the α-helix and β-sheet contents in the Col–HAp interaction decreased noticeably from 13.5% and 76.5% in native Col protein to 1.0% and 45.6%, respectively, but the proportion of random coils and turns increased considerably. The changes from ordered to disordered structures reveals that the binding of calcium and phosphate ions from HAp to the carbonyl and amide groups of Col protein disrupt the internal hydrogen-bonding network responsible for sustaining the folded triple helix structure. Consequently, the Col chains experience partial unfolding, leading to greater structural flexibility and exposure of reactive sites such as –NH and –COOH groups. These open residues trigger stronger interfacial bonding with the mineral phase of HAp, promoting Col–HAp integration and improving the composite's biomineralization potential and mechanical cohesion. The unfolding of Col protein from altering its native secondary structure, is not detrimental but rather adaptive, it enables the molecular reorganization necessary for organic-inorganic coupling. Such controlled unfolding transitions have been observed in biomimetic systems where Col interacts with inorganic phases to form hybrid materials resembling natural bone. Hence, the CD analysis suggests that the inclusion of HAp induces partial unfolding and refolding dynamics, in which Col protein loses part of its ordered triple–helical structure but simultaneously reorganizes into a more flexible and reactive conformation. This structural adaptation improves the scaffold's durability to regulate molecular interactions and diffusion pathways, enabling it to a effectively act as a natural bone mineralization while also providing a stable and responsive matrix for controlled and sustained drug delivery in regenerative applications.

### 3.5. Degradation study of scaffold in collagenase enzymatic medium

The degradation behaviour of the fabricated scaffold is monitored in a room temperature under a collagenase enzymatic medium prepared in phosphate buffer saline (PBS, pH 7.4) at a concentration of 0.2 mg $mL^{-1}$ is shown in Fig. 5(B). A gradual increase in degradation percentage was observed for all samples with increasing incubation time, indicating time-dependent enzymatic hydrolysis of the collagen-based matrix. Among the prepared scaffolds, Col–HAp (2 : 1) exhibited the highest degradation rate, reaching 81.5% mass loss after 24 h, whereas Col–HAp/h-BN (1 : 2 : 1) demonstrated the slowest degradation, with only about 20.91% mass loss within the same period. The relatively faster degradation of the Col–HAp (2 : 1) scaffold can be attributed to its higher Col protein content, which renders the matrix more susceptible to collagenase enzyme attack. Col protein, being a natural biopolymer, experiences a enzymatic cleavage through hydrolysis of its peptide bonds, leading to structural disintegration and weight loss. In contrast, the introduction of h-BN nanomaterial significantly reduced the degradation rate of the composite scaffolds. Both Col–HAp/h-BN (1 : 2 : 1) and Col–HAp/h-BN (2 : 1 : 1) exhibited noticeably higher structural stability compared to their h-BN free counterparts. This can be explained by the strong interfacial interactions between h-BN, Col protein and HAp, which create a more compact and crosslinked matrix that resists enzymatic attack. The planar h-BN nanosheets likely form hydrogen bonds with Col protein and electrostatic interactions with HAp, thus reducing the number of exposed Col sites available for enzymatic cleavage. Furthermore, the decrease in porosity of the h-BN incorporated scaffolds (6–7%) limits water diffusion and enzyme penetration, effectively slowing down the degradation process. Similar findings have been reported in silica- or graphene oxide-reinforced Col–HAp scaffolds, where nanofillers enhance structural durability by filling microvoids and stabilizing the polymer–ceramic interface.[38–40] The observed degradation trend thus follows the following order:

Col–HAp (2 : 1) > Col–HAp/h-BN (2 : 1 : 1) > Col–HAp (1 : 2) > Col–HAp/h-BN (1 : 2 : 1)

This pattern indicates that the combined influence of composition, porosity, and interfacial reinforcement leads to the enzymatic stability of the scaffolds. The slower degradation rate of Col–HAp/h-BN (1 : 2 : 1) confirms that the incorporation of h-BN reflects greater resistance to enzymatic digestion while maintaining sufficient biodegradability for tissue integration. Such controlled degradation is crucial for bone tissue engineering, as it allows the scaffold to retain mechanical strength during the initial healing phase and gradually degrade in synchrony with new bone matrix deposition. The results indicate that h-BN acts as a stabilizing nanofiller, enhancing matrix compactness and controlling scaffold degradation which is an essential feature for sustained drug delivery applications. The denser microstructure of the h-BN reinforced scaffolds can regulate drug diffusion, enabling a steady and prolonged release profile. Additionally, the tailored porosity and surface chemistry of the composite scaffold improve drug loading efficiency and adsorption stability, making the Col–HAp/h-BN scaffold a promising platform for combined bone regeneration and localized therapeutic delivery.

### 3.6. Drug load and release study of the scaffold

The drug loading and release behaviour of the fabricated scaffold was systematically investigated using ciprofloxacin (CIP) as a model therapeutic agent. In this study only Col–HAp/h-BN (1 : 2 : 1) is used for the study of drug load and release study, as it has the highest compressive strength and high surface area with low pore radius. Such scaffold is useful for control drug release. The study was designed to evaluate the suitability of the scaffold for localized drug delivery platform. Such scaffolds are expected to simultaneously provide mechanical stability, promote tissue regeneration, and deliver therapeutic molecules to prevent infection and accelerate healing. The kinetics of drug load and release were examined by following 1st order and 2nd order rate eqn (3) and (4):

$$\ln\left(\frac{C_0}{C_t}\right) = k_1 t \quad (3)$$

$$\left(\frac{1}{C_t}\right) - \left(\frac{1}{C_0}\right) = k_2 t \quad (4)$$

where $C_0$ and $C_t$ are the initial and final concentration of the drug molecules, $t$ denotes the exposure time, $k_1$ signifies the 1st order reaction rate kinetics and $k_2$ represents the 2nd order reaction rate kinetics.[41] To initiate drug loading, the Col–HAp/h-BN (1 : 2 : 1) scaffold were first activated using a 0.5 M acetic acid solution, a process intended to enhance the reactivity of the scaffold surface by increasing the number of available binding sites. The activation step is particularly effective in Col protein-based systems, as it alters the proteinaceous matrix and exposes supplementary amine and carboxyl groups capable of interacting with drug molecules. After activation, the scaffolds were dried and subsequently immersed in CIP solution (0.01 mg $mL^{-1}$). The uptake of CIP was quantitatively monitored at 30 min intervals using UV-Vis spectrophotometry as shown in Fig. 6(A), with changes in the solution absorbance intensity reflecting the amount of drug adsorbed by the scaffold. The first-order kinetic plot shown in Fig. 6(C) exhibits an excellent linear correlation ($R^2$ = 0.9995), confirming that the drug loading process follows first-order kinetics with a rate constant ($K$) value of 0.0719 $h^{-1}$. The results revealed a progressive decrease in absorbance intensity of the CIP solution with increasing immersion time, indicating continuous drug uptake by the scaffolds. This trend confirms that the Col–HAp/h-BN (1 : 2 : 1) scaffold possesses excellent drug loading ability, which can be attributed to both surface adsorption and entrapment within its porous microstructure. Col protein, the organic polymeric component, provides functional groups such as hydroxyl, amine, and carboxyl moieties that form hydrogen bonds and electrostatic interactions with CIP. HAp, the inorganic phase, further contributes through ionic interactions involving its calcium-rich sites and negatively charged phosphate groups. Meanwhile, the incorporation of h-BN nanofillers increases the available surface area and introduces additional adsorption pathways due to its layered structure and high stability. The porosity of a scaffold plays a crucial role in enhancing drug loading, highlighting its significance in the overall performance of the material. The lyophilization technique employed during scaffold fabrication generated a highly porous and interconnected network, allowing deeper penetration of the drug solution and

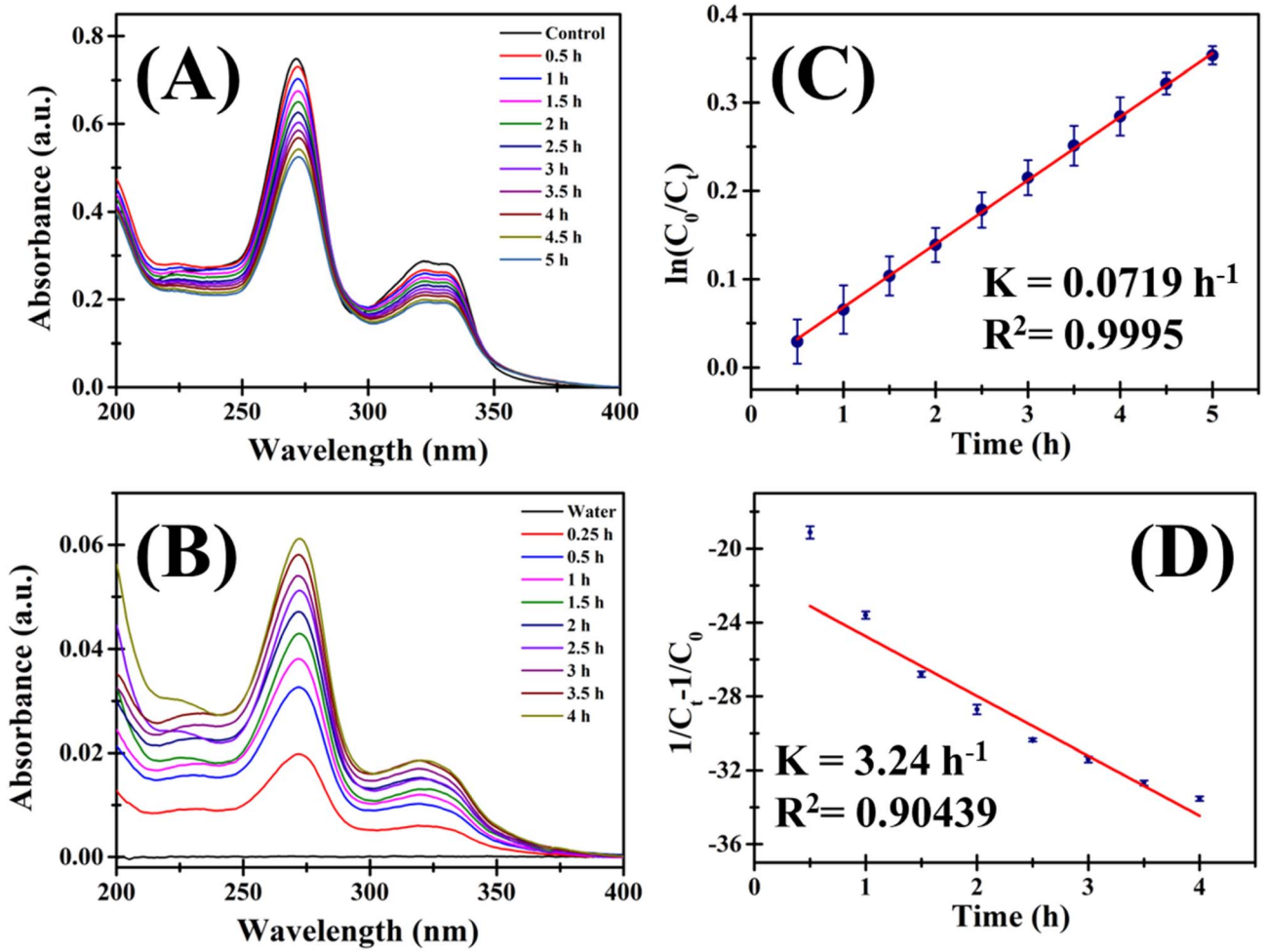


Fig. 6 UV-Vis spectra of drug (A) load and (B) release; (C) first-order kinetic plot of $\ln(C_0/C_t)$ *vs.* time for drug loading and (D) second-order kinetic plot of $(1/C_t - 1/C_0)$ *vs.* time for drug release.

ensuring uniform distribution of CIP throughout the matrix. Such homogeneity is desirable for sustained therapeutic delivery, as uneven loading often leads to rapid release or localized concentration spikes.[3] The present results suggest that the freeze-dried porous architecture significantly contributes to the scaffold's superior performance in drug entrapment, making it a promising carrier for a therapeutic agent.

After the drug loading phase, the release profile of CIP from the scaffold was evaluated by immersing the drug-loaded scaffold in distilled water (pH = 7) and monitoring the absorbance intensity of released molecules over time using UV-Vis spectrophotometry. As like in the loading phase, where a decrease in absorbance confirmed drug uptake, here a gradual increase in absorbance intensity was observed, reflecting the diffusion of CIP into the release medium. This release profile provided clear evidence that the scaffold not only encapsulate drug molecules efficiently but also allows their controlled release into the surrounding environment. The release pattern of CIP from the Col–HAp/h-BN (1 : 2 : 1) scaffold followed a biphasic trend commonly observed in porous biomaterials as shown in Fig. 6(B). An initial burst release was noted during the early immersion period, which can be attributed to the desorption of loosely bound or surface-adsorbed drug molecules. This rapid release is particularly beneficial in bone tissue engineering applications, where immediate antibacterial activity is required to prevent postoperative infections at the defect site. Following this initial stage, a sustained and gradual release was observed, corresponding to the diffusion of drug molecules from deeper within the scaffold matrix and their slow desorption from specific binding sites. Such a sustained release profile is beneficial for maintaining therapeutic concentrations of the drug over an extended period, thereby reducing the need for repeated administration and minimizing systemic side effects. The second-order kinetic plot shown in Fig. 6(D) for the drug release process exhibits a linear correlation with a rate constant ($K$) of 3.24 $h^{-1}$ and a correlation coefficient ($R^2$) of 0.90439.

The efficiency of the Col–HAp/h-BN (1 : 2 : 1) scaffolds as a therapeutic drug delivery platform can also be attributed to their multifunctional material composition. Col protein's hydrophilicity promotes diffusion, HAp contributes to sustained binding and slow release, and h-BN enhances structural stability, preventing premature scaffold degradation and ensuring long-term release. Together, these characteristics establish a favorable balance between rapid antibacterial action and long-term therapeutic support, a feature highly desirable for bone regeneration applications where prolonged healing times are common. The demonstrated drug-loading efficiency and controlled release kinetics suggest that the scaffold can be customized for other clinical applications, such as the inclusion of osteogenic factors to promote bone tissue formation or anticancer drug delivery for treating bone tumours. In addition, the tunability of scaffold composition and pore structure opens wide possibilities for tailoring drug release rates to specific therapeutic windows. The drug loading and release profile confirms that the fabricated scaffold is an effective multifunctional biomaterial, capable of incorporating CIP efficiently and releasing it in a controlled manner over time. The integration of Col, HAp and h-BN, develop a porous architecture achieved *via* lyophilization, providing the scaffold with excellent potential as a sustained delivery platform for therapeutic agents. These promising results highlight the fabricated scaffold as a strong candidate for future translational studies aimed for different clinical applications in bone defect repair and infection management.

### 3.7. Mechanism of drug load/release by the scaffold

The Scheme 2 illustrates the drug loading and release mechanism of the Col–HAp/h-BN (1 : 2 : 1) composite scaffold using CIP as the model drug. During the drug loading phase, a variety of physicochemical interactions align to the immobilization of CIP molecules within the composite framework. The Col protein which is abundance in amide and amino groups, forms electrostatic interactions and hydrogen bonding with CIP drug molecules, resulting in a physically stable and crosslinked network. These interactions strengthen the scaffold structure and enhance its capacity to retain the drug. The HAp which has large surface area and rich of $Ca^{2+}$ ions, acts as an efficient adsorption site for the anionic and polar functional groups of CIP through ionic bonding and electrostatic attraction.[42] The keto and carboxylate groups of CIP established ionic linkages with the positively charged $Ca^{2+}$ ions of HAp,[43] while the phosphate groups additionally emphasize the electrostatic stabilization of the adsorbed molecules.[44] Furthermore, the inclusion of h-BN nanomaterial presents the hydrophobic stacking and π–π interactions with the aromatic rings of CIP, providing additional non-covalent adsorption sites and further enhancing the drug encapsulation capacity. The integrated effect of Col, HAp, and h-BN creates a robust and porous composite matrix capable of sustaining a high drug loading capacity.

During drug release phase, the scaffold initiates to cooperate with nearby water molecules, introducing gradual bond dissociation and structural relaxation. Water molecules break the weak ionic bonds, hydrogen bonds, and electrostatic interactions, as indicated by the dotted lines in the Scheme 2. The CIP molecules detached from the scaffold surface into the surrounding aqueous medium. The release mechanism can be attributed to the diffusion-controlled process, in which the swelling and hydration of Col protein take place to facilitate the movement of water into the scaffold, thereby allowing CIP molecules to diffuse to outward environment from the porous network of the scaffold. The dissolution and ion exchange occurring at the HAp interface further contributes to the controlled desorption of CIP drug molecules, maintaining a sustained and control releasing of the CIP drug molecules. The role of porosity is significant, as the interconnected pores and hydrophilic nature of the scaffold emphasis efficient drug mobility, water uptake, and prolonged release kinetics.[45] The schematic diagram displays the drug release process involving progressive bond weakening, transforming the initially stable, multi-interaction drug-loaded structure into a hydrated, partially disassembled network. The Scheme 2 illustrates a comprehensive mechanism in which the combination of ionic, hydrogen, electrostatic, and hydrophobic interactions ensures effective drug immobilization, while the

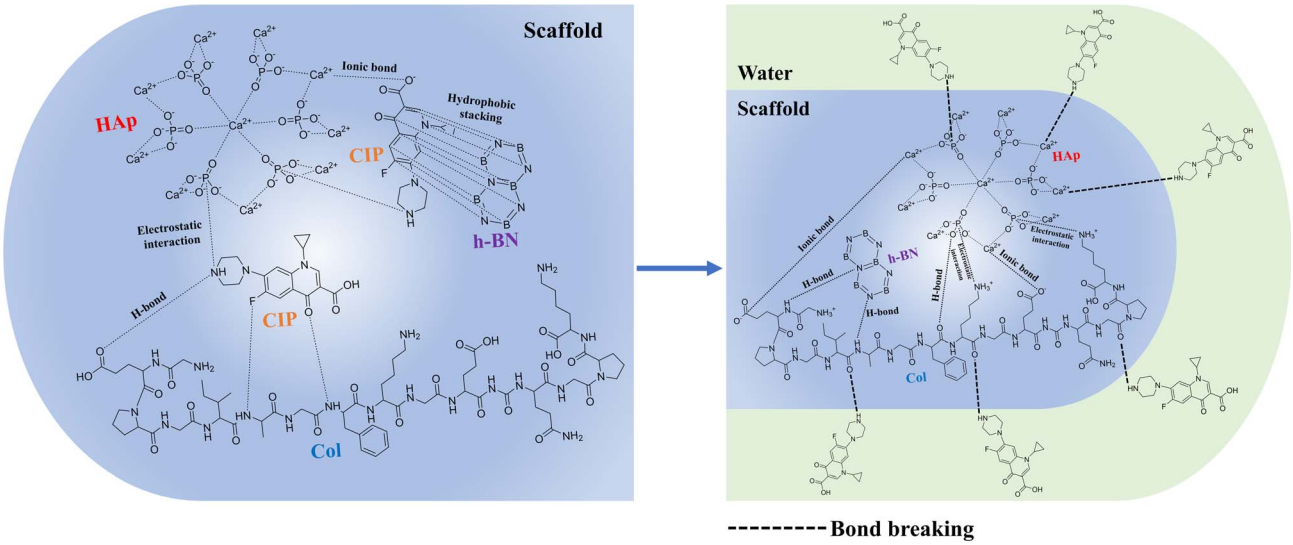


Scheme 2 Schematic representation of the drug loading and release mechanism of the fabricated scaffold using ciprofloxacin (CIP).

hydrophilicity and structural flexibility of the scaffold enable a sustained and controlled release of CIP. The multi-component interaction among Col, HAp, and h-BN not only enhances the mechanical stability of the scaffold but also provides a tunable platform for efficient drug delivery applications, making this hybrid material a promising candidate for biomedical and tissue engineering purposes.

### 3.8. Biocompatibility of the scaffold

The cell viability test was performed using the McCoy fibroblast cells cultured on the fabricated composite scaffolds namely Col–HAp (1 : 2), Col–HAp/h-BN (1 : 2 : 1), Col–HAp (2 : 1), and Col–HAp/h-BN (2 : 1 : 1) and was evaluated using the MTT assay after 24 h of incubation time and is shown in Fig. 7. The control group exhibited 100% viability, while the composite scaffolds displayed slightly varied but comparable results, with Col–HAp (1 : 2) showing 86.2 ± 30.7%, Col–HAp/h-BN (1 : 2 : 1) exhibiting the highest viability at 95.4 ± 32.3%, Col–HAp (2 : 1) at 87.2 ± 17.7%, and Col–HAp/h-BN (2 : 1 : 1) at 91.8 ± 24.5%. All fabricated scaffolds exhibited cell viability above 85%, indicating the absence of cytotoxicity and confirming their biocompatibility with fibroblast cells.[46] The highest cell viability of 95.4% for the Col–HAp/h-BN (1 : 2 : 1) scaffold suggested that the integration of Col, HAp and h-BN in this ratio provided an optimal microenvironment for cell survival and proliferation. The enhanced viability can be attributed to the balanced composition that ensured adequate bioactivity from HAp, cell adhesion support from Col, and improved surface characteristics from h-BN.[47] The inclusion of h-BN in a moderate concentration likely improved surface roughness and charge uniformity, thereby facilitating effective cell attachment. The 2D structure of h-BN may have promoted improved interfacial compatibility and better nutrient exchange within the polymer–ceramic matrix.[34,48] In comparison, the Col–HAp (1 : 2) and Col–HAp (2 : 1) scaffolds, although biocompatible, exhibited slightly lower viability values, which may be attributed to the non-inclusion of h-BN, resulting in less favourable surface interactions. The Col–HAp/h-BN (2 : 1 : 1) composite also showed high viability of 91% but the marginal reduction compared to the Col–HAp/h-BN (1 : 2 : 1) sample could be due to a higher Col content that potentially altered matrix stiffness or reduced mechanical stability, thereby affecting cellular response. Overall, the results indicated that the incorporation of h-BN within the Col–HAp matrix enhanced cell proliferation without inducing toxicity. However, the present cytocompatibility evaluation is only a preliminary assessment and future studies incorporating multiple relevant cell types, cell–material interaction imaging, and extended biological assays are essential to provide a more comprehensive understanding of scaffold biocompatibility.

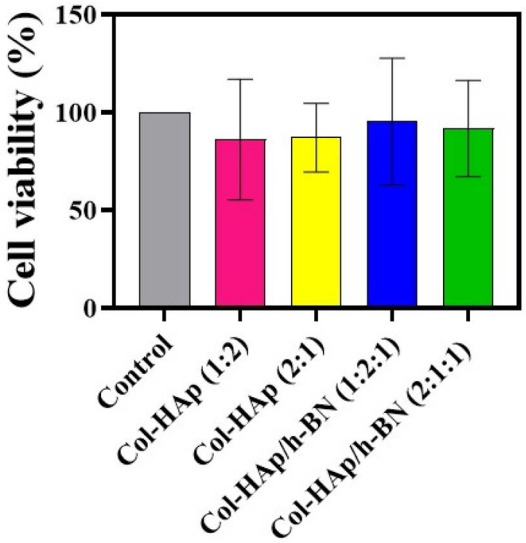


Fig. 7 Percentage of cell viability of McCoy cells in the presence of fabricated scaffolds after 24 h, with significance $P < 0.0001$.

## 4. Conclusion

In conclusion, the present work established the successful fabrication of Col–HAp composite scaffolds in the presence and absence of h-BN nanomaterial through a lyophilization technique, revealing in a functionally efficient and structurally stable biomaterial. The lyophilization process enabled the development of a interconnected porous structure, while the incorporation of h-BN led to a prominent enhancement in a surface activity, mechanical strength, and overall structural integrity, contributing to improved adsorption capacity and durability. CD spectroscopy confirmed the conformational behaviour of the secondary structure of Col protein, displaying that the lyophilization method sustained its native conformation and biological activity. The scaffold also signifies improved thermal stability upon addition of h-BN, confirming its ability to sustain structural robustness under both the physiological and elevated temperature conditions. In addition, the enzymatic degradation studies in a collagenase enzyme medium demonstrates high degradation pattern in case of high Col protein content within scaffold matrix, signifying the scaffold's-controlled biodegradability and its suitability for long-term biomedical applications. Drug loading and release profile of the scaffold using ciprofloxacin (CIP) followed first-order and second-order kinetics, respectively, displaying a diffusion-mediated mechanism regulated by the scaffold's internal microstructure. The fabricated scaffolds also display an excellent biocompatibility and high cell viability, confirming their non-toxic and cytocompatibility nature. Furthermore, the lyophilized h-BN incorporated Col–HAp scaffold exhibits a balanced combination of mechanical integrity, enhanced surface characteristics, thermal and enzymatic stability, and biological safety, making it a highly promising candidate for controlled drug delivery, tissue regeneration, and advanced biomedical engineering applications.

## Conflicts of interest

There is no conflicts of interest to declare.

## Data availability

The datasets used and/or analyzed during the current study are available from the corresponding author on reasonable request.

Supplementary information (SI): adsorption–desorption isotherms of all scaffold; compressive stress *vs.* strain curve of all fabricated scaffold. See DOI: https://doi.org/10.1039/d5ra09090c.

## Acknowledgements

BB thank Council of Scientific and Industrial Research, India for the fellowship. RS thank University Grants Commission, New Delhi for the fellowship. Authors acknowledge IASST, Guwahati for in-house project. The authors thank SAIC-IASST, Guwahati for providing instrumentation facilities.

## References

1 T. Garg, O. Singh, S. Arora and R. S. R. Murthy, *Crit. Rev. Ther. Drug Carrier Syst.*, 2012, **29**, 1–63.
2 M. S. B. Reddy, D. Ponnamma, R. Choudhary and K. K. Sadasivuni, *Polymers*, 2021, **13**, 1105.
3 A. Zielińska, J. Karczewski, P. Eder, T. Kolanowski, M. Szalata, K. Wielgus, M. Szalata, D. Kim, S. R. Shin, R. Słomski, E. B. Souto and J. Contr, *Release*, 2023, **359**, 207–223.
4 J. Bielajew, J. C. Hu and K. A. Athanasiou, *Nat. Rev. Mater.*, 2020, **5**, 730–747.
5 H. Xie, S. Ruan, M. Zhao, J. Long, X. Ma, J. Guo and X. Lin, *RSC Adv.*, 2023, **13**, 23010–23020.
6 F. Fendi, B. Abdullah, S. Suryani, A. N. Usman and D. Tahir, *Bone*, 2024, **183**, 117075.
7 J. Venkatesan, P. A. Vinodhini, P. N. Sudha and S.-K. Kim, *Adv. Food Nutr. Res.*, 2014, **73**, 59–81.
8 W. Yu, T.-W. Sun, C. Qi, Z. Ding, H. Zhao, S. Zhao, Z. Shi, Y.-J. Zhu, D. Chen and Y. He, *Int. J. Nanomed.*, 2017, **12**, 2293–2306.
9 Y. Zhao, T. Fan, J. Chen, J. Su, X. Zhi, P. Pan, L. Zou and Q. Zhang, *Colloids Surf., B*, 2018, **174**, 70–79.
10 F. Liu, H. Kang, Z. Liu, S. Jin, G. Yan, Y. Sun, F. Li, H. Zhan and Y. Gu, *Nanomaterials*, 2021, **11**, 2456.
11 Y. Vangolu and M. T. Yurtcan, *Ceram. Int.*, 2021, **47**, 32969–32978.
12 A. A. Musa, A. Bello, S. M. Adams, A. P. Onwualu, V. C. Anye, K. A. Bello and I. I. Obianyo, *Polymers*, 2025, **17**, 893.
13 A. Hasan, M. Morshed, A. Memic, S. Hassan, T. Webster and H. Marei, *Int. J. Nanomed.*, 2018, **13**, 5637–5655.
14 N. E. Duygulu, M. Balkas, F. Ciftci and M. Kucak, *Macromol. Mater. Eng.*, 2025, **310**, e00066.
15 S. Nagarajan, H. Belaid, C. Pochat-Bohatier, C. Teyssier, I. Iatsunskyi, E. Coy, S. Balme, D. Cornu, P. Miele, N. S. Kalkura, V. Cavaillès and M. Bechelany, *ACS Appl. Mater. Interfaces*, 2017, **9**, 33695–33706.
16 S. R. Stock, *Calcif. Tissue Int.*, 2015, **97**, 262–280.
17 N. Angraini, S. Syarifuddin, N. Rauf and D. Tahir, *Artif. Organs*, 2025, **49**, 1236–1248.
18 A. G. González, M. R. Santana, P. De Carmen Zambrano Robledo and R. Quiza, *MRS Adv.*, 2022, **7**, 1212–1217.
19 J. Upadhyaya, I. R. Singh, B. Pun, H. J. Baishya, S. Kumar, S. R. Joshi and S. Mitra, *J. Phys. Chem. B*, 2025, **129**, 1274–1288.
20 R. Nazir, A. Bruyneel, C. Carr and J. Czernuszka, *J. Funct. Biomater.*, 2021, **12**, 20.
21 J. Van Meerloo, G. J. L. Kaspers and J. Cloos, *Methods Mol. Biol.*, 2011, **731**, 237–245.
22 P. Kumar, A. Nagarajan and P. D. Uchil, *Cold Spring Harb. Protoc.*, 2018, **2018**, 95505.
23 M. M. Villa, L. Wang, J. Huang, D. W. Rowe and M. Wei, *J. Biomed. Mater. Res., Part B*, 2014, **103**, 243–253.
24 Z. Ebrahimi, S. Irani, A. Ardeshirylajimi and E. Seyedjafari, *Sci. Rep.*, 2022, **12**, 12359.
25 M. A. Bryan, J. W. Brauner, G. Anderle, C. R. Flach, B. Brodsky and R. Mendelsohn, *J. Am. Chem. Soc.*, 2007, **129**, 7877–7884.

26 M. C. Chang and J. Tanaka, *Biomaterials*, 2002, **23**, 4811–4818.
27 L. A. F. Vieira, J. P. N. Marinho, M. A. Rodrigues, J. P. B. De Souza, R. G. De Sousa and E. M. B. De Sousa, *Ceram. Int.*, 2024, **50**, 32064–32080.
28 G. M. Cunniffe, G. R. Dickson, S. Partap, K. T. Stanton and F. J. O'Brien, *J. Mater. Sci.: Mater. Med.*, 2009, **21**, 2293–2298.
29 J. Becerra, M. Rodriguez, D. Leal, K. Noris-Suarez and G. Gonzalez, *J. Mater. Sci.: Mater. Med.*, 2022, **33**, 18.
30 H. He, L. Wang, X. Cai, Q. Wang, P. Liu and J. Xiao, *Mater. Des.*, 2023, **236**, 112510.
31 R. Durga, N. Jimenez, S. Ramanathan, P. Suraneni and W. J. Pestle, *J. Archaeol. Sci.*, 2022, **145**, 105644.
32 A. Babakhani, S. J. Peighambardoust, M. Ghahremani-Nasab and N. S. Peighambardoust, *Sci. Rep.*, 2025, **15**, 22235.
33 F. Mukasheva, L. Adilova, A. Dyussenbinov, B. Yernaimanova, M. Abilev and D. Akilbekova, *Front. Bioeng. Biotechnol.*, 2024, **12**, 1444986.
34 V. S. Lahiri, A. P. Benaduce, S. Seal, L. Kos and A. Agarwal, *J. Mech. Behav. Biomed. Mater.*, 2010, **4**, 44–56.
35 J. Wang, Z. Zhang, G. Su, X. Sun, Y. Wang, Z. Fang, M. Chen, Q. Zhang and J. Biomater, *Tissue Eng.*, 2017, **7**, 1000–1007.
36 M. G. Mejia, D. F. Hincapie-Rojas, F. N. Jimenez-Garcia and C. A. A. Vargas, *Heliyon*, 2023, **9**, e13567.
37 C. M. Stultz, *Protein Sci.*, 2006, **15**, 2166–2177.
38 M. Li, P. Xiong, F. Yan, S. Li, C. Ren, Z. Yin, A. Li, H. Li, X. Ji, Y. Zheng and Y. Cheng, *Bioact. Mater.*, 2018, **3**, 1–18.
39 M. Sumathra, M. A. Munusamy, A. A. Alarfaj and M. Rajan, *Biomed. Pharmacother.*, 2018, **103**, 858–868.
40 M. Ahmadipour, H. Mohammadi, A. L. Pang, M. Arjmand, T. A. Otitoju, P. U. Okoye and B. Rajitha, *Int. J. Polym. Mater.*, 2020, **71**, 180–195.
41 N. J. Mondal, R. Sonkar, B. Boro, M. P. Ghosh and D. Chowdhury, *Nanoscale Adv.*, 2023, **5**, 5460–5475.
42 P. S. Guru, B. Panda and K. N. Parida, *Next Mater.*, 2025, **9**, 101042.
43 M. Kara, B. Hasinoff, D. McKay and N. Campbell, *Br. J. Clin. Pharmacol.*, 1991, **31**, 257–261.
44 Y. C. Wang, L. M. Ma, H. J. Xue, J. F. Qiu, M. Zhang, G. Y. Xiao and Y. P. Lu, *Dalton Trans.*, 2025, **54**, 10227–10233.
45 J. L. Hernandez and K. A. Woodrow, *Adv. Healthcare Mater.*, 2022, **11**, e2102087.
46 M. Andonegi, K. L. Heras, E. Santos-Vizcaíno, M. Igartua, R. M. Hernandez, K. De La Caba and P. Guerrero, *Carbohydr. Polym.*, 2020, **237**, 116159.
47 A. Tozar and İ. H. Karahan, *Appl. Surf. Sci.*, 2018, **452**, 322–336.
48 C. Wang, J. Feng, J. Zhou, X. Huang, L. Wang, G. Liu and J. Cheng, *J. Mater. Sci.*, 2020, **55**, 14501–14515.